Effects of anisotropic viscosity and texture development on convection in ice mantles

M. L. Rudolph[1] and M. Manga[1]

Received 22 June 2012; revised 24 September 2012; accepted 27 September 2012; published 7 November 2012.

[1] Convection may occur in the ice shells of satellites in the outer solar system. The style of convection, rate of heat transport, and resulting surface features depend on the rheology of ice, which in turn depends on temperature, grain size, stress, and crystallographic preferred orientation (CPO). Here we study the effect of CPO development and anisotropic viscosity on convection by coupling a model of polycrystalline ice deformation with a macroscopic flow model. Despite having a first-order effect on velocities and heat transport in a convecting ice shell, fabric development is unlikely to be observable either directly by spacecraft-based radar or indirectly based on changes in the wavelength or amplitude of dynamic topography.

Citation: Rudolph, M. L., and M. Manga (2012), Effects of anisotropic viscosity and texture development on convection in ice mantles, *J. Geophys. Res.*, *117*, E11003, doi:10.1029/2012JE004166.

1. Introduction

[2] The ice mantles of satellites in the outer solar system may transport heat by solid-state convection. Convection affects the thermal and rheological structure of a planetary ice shell, with implications for the location and amount of tidal dissipation, the elastic layer thickness, the stress state in the elastic layer, and for surface tectonic and flexural features. The occurrence and style of convection depend on rheology. Below pressures of 2×10^8 Pa and above $\sim$72 K, ice Ih is the stable phase of water ice. Under some temperature and stress conditions, ice Ih crystals deform most easily by basal slip (occurring on planes perpendicular to the crystal's *c* axis, the axis of sixfold symmetry). The resolved shear stress on the basal planes depends on the orientation of the ice crystal, and hence the single crystal has anisotropic viscosity. When polycrystalline ice develops crystallographic preferred orientation (CPO), the ice has anisotropic viscosity [e.g., *Cuffey and Paterson*, 2010].

[3] Understanding and identifying current or past convection is important for three reasons. First, convection affects the overall rate of heat transport and governs thermal evolution [*Consolmagno and Lewis*, 1978; *McKinnon*, 1999; *Ruiz and Tejero*, 2003; *Barr et al.*, 2004; *Mitri and Showman*, 2005; *Freeman et al.*, 2006; *Barr and McKinnon*, 2007a; *Roberts and Nimmo*, 2008; *Ruiz*, 2010; *Travis et al.*, 2012], and consequently, the rheological properties of an icy body. In turn, temperature and rheology affect the location and amount of tidal dissipation [*Hussmann et al.*, 2002; *Sotin et al.*, 2002; *Tobie et al.*, 2003; *Moore*, 2006; *Mitri and Showman*, 2008; *Běhounková et al.*, 2010; *Han and Showman*, 2010]. Second, convection may produce some of the surface features observed on icy bodies. For instance, Europa's ridges [*Han and Showman*, 2008], pits [*Showman and Han*, 2004] and domes [*Rathbun et al.*, 1998; *Pappalardo et al.*, 1998; *Nimmo and Manga*, 2002; *Pappalardo and Barr*, 2004; *Han and Showman*, 2005; *Ruiz et al.*, 2007], and chaos features [*Schenk and Pappalardo*, 2004; *Showman and Han*, 2005] have been linked to convective processes. Third, convection transports mass vertically and may carry material from a subsurface ocean to the near surface or create conditions that allow other processes to transport this material to the surface [*Fagents et al.*, 2000; *Manga and Wang*, 2007; *Rudolph and Manga*, 2009].

[4] Here, we study how convection is affected by the development of crystallographic preferred orientation (CPO) and the resulting viscous anisotropy. We describe an anisotropic viscoplastic model linking single-crystal deformation to polycrystal deformation. Next, we present a method to include the polycrystal deformation model within geodynamic models and present the results of numerical simulations. We discuss the implications of these simulations in the context of whether the resulting features might be detectable and whether fabric development affects topographic features and thermal evolution of icy satellites.

2. Methods

[5] In order to model the deformation of textured polycrystalline ice, we first describe a model linking grain-scale deformation to macroscopic stress and strain. We then include the microscale model in a macroscopic convection calculation in which we employ Lagrangian tracer particles

[1]Department of Earth and Planetary Science, University of California, Berkeley, California, USA.

Corresponding author: M. L. Rudolph, Department of Earth and Planetary Science, University of California, 307 McCone Hall, Berkeley, CA 94720, USA. (rudolph@berkeley.edu)

0148-0227/12/2012JE004166

to track texture. The constitutive laws typically used in ice sheet modeling take the form [*Cuffey and Paterson*, 2010]

$$\dot{\epsilon}_{ij} = A\tau^{n-1}\sigma^D_{ij} \tag{1}$$

where $\tau = \sqrt{\frac{1}{2}\mathrm{II}_{\sigma^D}}$ and II_{σ^D} is the second deviatoric stress invariant, σ^D is the deviatoric stress tensor, and $\underline{\dot{\epsilon}}$ is the strain rate tensor. The term A depends foremost on temperature, as well as pressure, melt fraction, the presence of impurities, and grain size for some creep mechanisms. The key features of equation (1) are that if $n \neq 1$ a nonlinear relationship exists between stress and strain rate and that if the effective stress τ is known, $\dot{\epsilon}_{ij}$ depends only on σ^D_{ij} and not any other components of the stress tensor. Fluids with anisotropic viscosity have constitutive equations of the form

$$\dot{\epsilon}_{ij} = M_{ijkl}\sigma^D_{kl} \tag{2}$$

where $\underline{\underline{M}}$ is a fourth rank tensor that is, in general, a nonlinear function of stress, temperature, grain size, and fabric.

2.1. Model for Polycrystal Deformation and Texture Development

[6] We write the single-crystal stress and strain rate tensors s and d and the polycrystal stress and strain rate tensors S and D following the notation of *Castelnau et al.* [1996]. The rate of shear on a slip system s is

$$\dot{\gamma}^s = \gamma_0\left|\frac{\underline{r}^s : \underline{s}}{\tau^s_0}\right|^{n^s-1}\frac{\underline{r}^s : \underline{s}}{\tau^s_0} \tag{3}$$

where $r^s = b \otimes n$ is the Schmid tensor for slip system s, b is the Burgers vector and n the unit normal to slip system s, n^s is the power law exponent (equation (1)) for slip system s, $\otimes$ denotes the tensor product [e.g., *Chadwick*, 1999], γ^s_0 and τ^s_0 are reference slip rate and stress, and the colon denotes he tensor inner product ($\underline{a} : \underline{b} = a_{ij}b_{ij}$). Temperature dependence enters through the term $\dot{\gamma}_0$, which we modify to take the form $\dot{\gamma}^s_0/\left(\tau^s_0\right)^{n^s} = \beta A(T)$, where $A(T) = A_0\exp(-Q/RT)$ [*Thorsteinsson*, 2002]. The single-crystal velocity gradient tensor l is computed from $\dot{\gamma}$ (equation (3)) by summation over all slip systems:

$$\underline{l} = \dot{\gamma}_0\sum_s \underline{r}^s\left|\frac{\underline{r}^s : \underline{s}}{\tau^s_0}\right|^{n^s-1}\frac{\underline{r}^s : \underline{s}}{\tau^s_0}. \tag{4}$$

[7] In order to relate single-crystal stress and strain to macroscopic stress and strain, we must make assumptions about how stress is distributed within the polycrystal, in particular whether and how much each grain affects its neighbors. Some closure relationships ignore neighbor interactions entirely, while others explicitly account for this effect [*Thorsteinsson*, 2002], which requires tracking the spatial distribution of individual crystals in addition to their orientation and shape. The *Thorsteinsson* [2002] model is attractive for our purposes because it captures the essential features of texture development through grain reorientation and compares favorably with viscoplastic self-consistent (VPSC) models [*Lebensohn and Tome*, 1993] with significantly reduced computational expense. *Thorsteinsson* [2002] introduces a relationship between single crystal and macroscopic stress tensors of the form

$$\underline{s} = \mathcal{E}^c\underline{S}. \tag{5}$$

The polycrystal is represented as a three-dimensional grid of crystals and $\mathcal{E}^c$ is a neighbor interaction term defined as

$$\mathcal{E}^c = \frac{1}{\zeta + 6\xi}\left(\zeta + \xi\sum_{i=1}^{6}\frac{\mathcal{T}^i}{\mathcal{T}^c}\right). \tag{6}$$

Here ζ and ξ are tuning parameters that control the strength of the neighbor interactions. Note that when $\zeta = 1$ and $\xi = 0$, $s = S$, recovering the uniform stress approximation [*Taylor*, 1938]. The superscript c denotes the crystal for which s is being computed and the summation index i denotes the six neighboring crystals (left, right, up, down, front, back) in the three-dimensional grid. The term $\mathcal{T}^i$ is a measure of the total resolved shear stress on all active slip systems in crystal i:

$$\mathcal{T}^i = \left|\sum_s \tau^s\hat{\underline{b}}^s\right| \tag{7}$$

and b^s is the Burgers vector for slip system s.

[8] Substituting equation (5) into equation (4), we obtain an expression for the single crystal velocity gradient:

$$\underline{l} = \dot{\gamma}_0\sum_s \underline{r}^s\mathcal{E}^c\left|\frac{\underline{r}^s : \underline{S}}{\tau^s_0}\right|^{n^s-1}\frac{\underline{r}^s : \underline{S}}{\tau^s_0}. \tag{8}$$

By assumption, the macroscopic velocity gradient is the volumetric average of the microscopic velocity gradients over N single crystals:

$$\underline{L} = \frac{1}{N}\sum_{c=1}^{N}\underline{l}. \tag{9}$$

[9] To obtain a numerically useful constitutive equation, we first combine equations (8) and (9):

$$\underline{L} = \frac{1}{N}\sum_{c=1}^{N}\dot{\gamma}_0\sum_s \underline{r}^s\mathcal{E}^c\left|\frac{\underline{r}^s : \underline{S}}{\tau^s_0}\right|^{n^s-1}\frac{\underline{r}^s : \underline{S}}{\tau^s_0}. \tag{10}$$

Noting that $\underline{r}\left(\underline{r} : \underline{S}\right) = \left(\underline{r}\otimes\underline{r}\right) : \underline{S}$,

$$\underline{L} = \left[\frac{1}{N}\sum_{c=1}^{N}\dot{\gamma}_0\sum_s\frac{\left(\underline{r}^s\otimes\underline{r}^s\right)}{\tau^s_0}\mathcal{E}^c\left|\frac{\underline{r}^s : \underline{S}}{\tau^s_0}\right|^{n^s-1}\right] : \underline{S} = \underline{\underline{M}}(\underline{S}) : \underline{S} \tag{11}$$

where $\underline{\underline{M}}(\underline{S})$ is a fourth rank tensor, conceptually identical to the elasticity tensor $\underline{\underline{C}}$, but which is in this case a nonlinear function of the macroscopic stress tensor S. The tensor inner product between mixed order tensors here is defined $\left(\underline{\underline{A}} : \underline{B}\right)_{ij} = A_{ijkl}B_{kl}$. The velocity gradient tensor L is related

Table 1. Summary of Model Parameters[a]

Symbol	Name	Case 1/Case 2
H	layer thickness	15 km/75 km
d	grain size	0.1 mm/1 mm
$Ra_{1,\mathrm{diff}}$	basal Rayleigh number[a]	2.2×10^7/2.6×10^7
ρ	density	930 kg m^{-3}
k	thermal conductivity	3.3 W m^{-1} K^{-1}
C_p	specific heat capacity	3548 J kg^{-1} K^{-1}
α	thermal expansivity	10^{-4} K^{-1}
g	gravitational acceleration	1.3 m s^{-2}
δT	initial temperature perturbation	15 K

[a] *Solomatov* [1995].

to strain rate $\underline{D} = \frac{1}{2}\left(\underline{L} + \underline{L}^T\right)$. Substitution of $\underline{\underline{M}}$ yields in index notation:

$$D_{ij} = \frac{1}{2}\left(M_{ijkl} + M_{jikl}\right)S_{kl} = M^S_{ijkl}S_{kl}. \qquad (12)$$

[10] In order to express stress in terms of strain rate, we take the common approach of vectorizing S and D and denote the vectorized stress and strain rate $\hat{\underline{S}}$ and $\hat{\underline{D}}$. The corresponding second-order equivalent of $\underline{\underline{M}}^S$ is $\hat{\underline{\underline{M}}}^S$, numerically a square matrix that can be inverted to yield $\hat{\underline{\underline{N}}} = \hat{\underline{\underline{M}}}^{S^{-1}}$, and $\hat{\underline{S}} = \underline{\underline{N}} \cdot \hat{\underline{D}}$, which can be used in the macroscopic numerical model.

[11] Finally, we introduce the time evolution of the crystal fabric. We express the rate of change in c axis orientation (c) as

$$\dot{\mathbf{c}} = \underline{w}\mathbf{c} \qquad (13)$$

where $\underline{w} = \frac{1}{2}\left(\underline{l} - \underline{l}^T\right)$ is the single-crystal rate of spin tensor. We also account for the rotation of the polycrystal by macroscopic flow.

2.2. Composite Rheology

[12] *Goldsby and Kohlstedt* [2001] proposed a composite rheology for ice of the form

$$D = D_{\mathrm{disl}} + \left(D^{-1}_{\mathrm{gbs}} + D^{-1}_{\mathrm{bs}}\right)^{-1} + D_{\mathrm{diff}}. \qquad (14)$$

The first term D_{disl} is negligible for the temperatures, stresses, and grain sizes considered here. One key feature of this proposed composite rheology is that the reciprocal grouping of grain boundary sliding (gbs) and basal slip (bs)strain rates allows either mechanism to limit the effectiveness of the other deformation mechanism. We introduce a scalar creep inhibition factor α to capture the effect of the reciprocal term in equation (14):

$$\alpha = \frac{\sqrt{\underline{D}_{\mathrm{gbs}} : \underline{D}_{\mathrm{gbs}}}}{\sqrt{\underline{D}_{\mathrm{bs}} : \underline{D}_{\mathrm{bs}}}} \qquad (15)$$

where $\underline{D}_{\mathrm{bs}}$ encompasses all of the deformation accounted for by our microscale model:

$$\underline{D} = \left(\frac{\alpha}{1+\alpha}\underline{D}_{\mathrm{bs}}\right) + \underline{D}_{\mathrm{diff}}. \qquad (16)$$

Recalling that $\underline{D}_{\mathrm{bs}} = \underline{\underline{M}} \cdot \underline{S}$, we introduce a modified visco-plasticity tensor $\underline{\underline{M}}'$ that accounts for all deformation mechanisms:

$$M'_{ijkl} = \frac{\alpha}{1+\alpha}M_{ijkl} + 2\delta_{ik}\delta_{jl}\eta_{\mathrm{diff}} \qquad (17)$$

where η_{diff} is the effective viscosity for diffusion creep. Because we model two-dimensional convection but the anisotropic viscous response is three-dimensional, we impose a constraint on the polycrystal to prohibit out of plane deformation.

[13] We calibrate the micro-macro model against the basal slip component of the *Goldsby and Kohlstedt* [2001] model. We assume temperature dependence of the form

$$\dot{\gamma}_0 = A_0 \exp(-Q/(RT))\left(\tau^s_0\right)^n. \qquad (18)$$

For basal slip, $n = 2$ is favored by *Castelnau et al.* [1997]. We choose $Q = 60$ kJ mol^{-1} [*Goldsby and Kohlstedt*, 2001]. We impose an isotropic initial fabric on a grid of 20 × 20 × 20 crystals at a temperature of −10°C and find a best fit value of $A_0 = 7.35 \times 10^{-4}$ Pa^{-2} s^{-1}. The effective viscosity for diffusion creep is chosen to be identical to that used by *Barr and Stillman* [2011]:

$$\eta_{\mathrm{diff}} = \frac{1}{2}\frac{3R_G T_b d^2}{42 V_m D_{0,v}}\exp\left(Q^*_V/(R_G T)\right). \qquad (19)$$

Here $V_m = 1.97 \times 10^{-5}$ m^{-3}, $D_{0,v} = 9.10 \times 10^{-4}$ m^2 s^{-1}, $Q^*_V = 59.4$ kJ mol^{-1}.

2.3. Macroscopic Flow Model

[14] We solve equations for the balance of momentum and mass conservation:

$$\begin{aligned} \rho\frac{\mathrm{D}\mathbf{u}}{\mathrm{D}t} &= -\nabla p + \nabla \cdot \underline{S}^D + \rho\mathbf{g} \\ \nabla \cdot \mathbf{u} &= 0 \end{aligned} \qquad (20)$$

and advection and diffusion of heat:

$$\rho C_p \frac{DT}{Dt} = \nabla \cdot (k\nabla T) \qquad (21)$$

with parameters defined in Table 1, using a conservative finite difference technique combined with a marker-in-cell approach [*Gerya and Yuen*, 2003] in two spatial dimensions. Each Lagrangian marker carries information about the local fabric (c axis orientations). The momentum equation is expressed in terms of velocity u:

$$\rho\frac{\mathrm{D}u_i}{\mathrm{D}t} = -\frac{\partial p}{\partial x_i} + \frac{\partial N_{ijkl}D_{kl}}{\partial x_j} + \rho g_i \qquad (22)$$

where p is pressure, ρ is density, and g_i are the components of gravitation acceleration. Parallelization was necessary

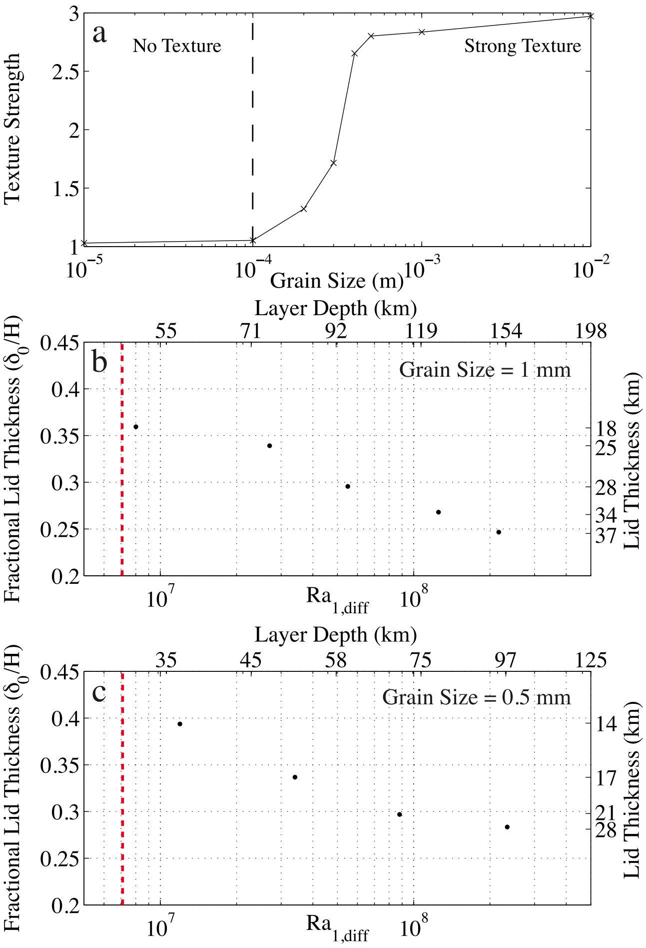

Figure 1. (a) Texture strength (S, defined in text), which increases rapidly between grain sizes of 10^{-4} m and 10^{-3} m. Stagnant lid thickness calculated from numerically versus $Ra_{1,\mathrm{diff}}$ (or equivalently layer thickness) (b) for a grain size of 1.0 mm and (c) for a grain size of 0.5 mm. Vertical red line indicates the critical layer thickness for convection to occur, calculated using a bisection method.

even for 2-D problems because calculating the polycrystal response for each Lagrangian tracer increases runtime by a factor of 100. The macroscopic flow model uses PETSc [*Balay et al.*, 2012] for domain decomposition and parallel communication. We solved the resulting linear system of equations using the parallel direct solver MUMPS [*Amestoy et al.*, 2001, 2006]. After performing resolution tests, we determined that the calculations could be performed on a 41×41 Eulerian grid with 25 Lagrangian markers per cell initially. We eliminated markers if more than 64 were present in one cell usingthe method described by *Leng and Zhong* [2011] and added markers (using nearest-neighbor interpolation) to any cell containing fewer than 10 markers.

2.4. Model Parameters

[15] We ran two-dimensional convection simulations in boxes twice as wide as they are deep. The top and bottom mechanical boundary conditions are free slip, and the lateral boundaries are periodic. The top and bottom are prescribed temperature (Dirichlet) with T = 100 K and T = 260 K. In each case, we run the model with the *Goldsby and Kohlstedt* [2001] rheology from an initial sinusoidal perturbation with amplitude δT = 15 K and wavelength equal to the domain width until a steady state, defined by constant Nusselt number (Nu) and root-mean-square velocity V_{rms} [*Blankenbach et al.*, 1989] and steady flow field, is reached. We then continue the simulation using the micro-macro rheology and an initially uniform isotropic fabric. All of the simulations considered feature a thick stagnant lid overlying a convecting subregion. The two cases that we discuss here are a 75 km thick layer with a grain size of 1 mm and a 15 km thick layer with a grain size of 0.1 mm. We assume uniform grain size in our model because our objective is to quantify the effects of anisotropic viscosity in isolation of other processes such as stress-induced grain reduction [*Barr and McKinnon*, 2007b]. Other model parameters are listed in Table 1.

3. Depth at Which CPO Develops

[16] We illustrate the grain size dependence of fabric strength in Figure 1a. We performed numerical polycrystal deformation experiments with $\sigma_{xx} = -\sigma_{yy} = 10^4$ Pa (all other stress components zero) and T = 250 K (representative of the warm convecting interior of an ice shell) until a strain of 1.0 was achieved. Next, we characterized the strength of the c axis fabric using the texture strength $S = \sqrt{\langle f^2 \rangle}$ [e.g., *Bunge*, 1982], where $f(\theta, \phi)$ is the probability density function of c axis orientations in the simulated polycrystal. A value of S = 1.0 indicates an isotropic fabric while higher values indicate development of CPO. For grain sizes smaller than about 0.1 mm, S is close to 1.0. S increases rapidly between grain sizes of 0.1 and 0.5 mm. In convection problems, Lagrangian tracers experience changing stresses as they are advected through a convection cell, and if macroscopic stress changes faster than crystals within the polycrystal can rotate in response to the applied stress, fabric formation can be limited [e.g., *Castelnau et al.*, 2009]. The texture in each of our simulations was steady when the simulations were terminated, and we attribute the steady texture to the competition between reorientation of crystals and changing macroscopic stress.

[17] In order to develop CPO, ice must deform by dislocation creep through strains of at least $\sim 10^{-1}$, with stronger fabrics requiring strains of $O(1)$. Strains of this magnitude are certainly attainable in the convecting interior of an ice shell but are not achieved in the stagnant lid. Figures 1b and 1c show how stagnant lid thickness varies as a function of $Ra_{1,\mathrm{diff}}$, or equivalently layer thickness (H), based on numerical simulations run to steady state with the isotropic *Goldsby and Kohlstedt* [2001] rheology. The diffusion creep Rayleigh number is defined as $Ra_{1,\mathrm{diff}} = \rho g \alpha \Delta T H^3/(\kappa \eta_{1,\mathrm{diff}})$ where $\kappa = k/(\rho C_p)$ is thermal diffusivity and $\eta_{1,\mathrm{diff}}$ is the effective viscosity for the diffusion creep deformation mechanism for the temperature and grain size at the base of the ice shell [*Solomatov*, 1995; *Barr et al.*, 2004]. We indicate the minimum layer thickness for which convection is possible for our model geometry and amplitude of initial temperature perturbation δT with vertical dashed lines in Figures 1b and 1c. The thickness δ_0 of the stagnant lid can be viewed as a lower bound on the depth at which texture will

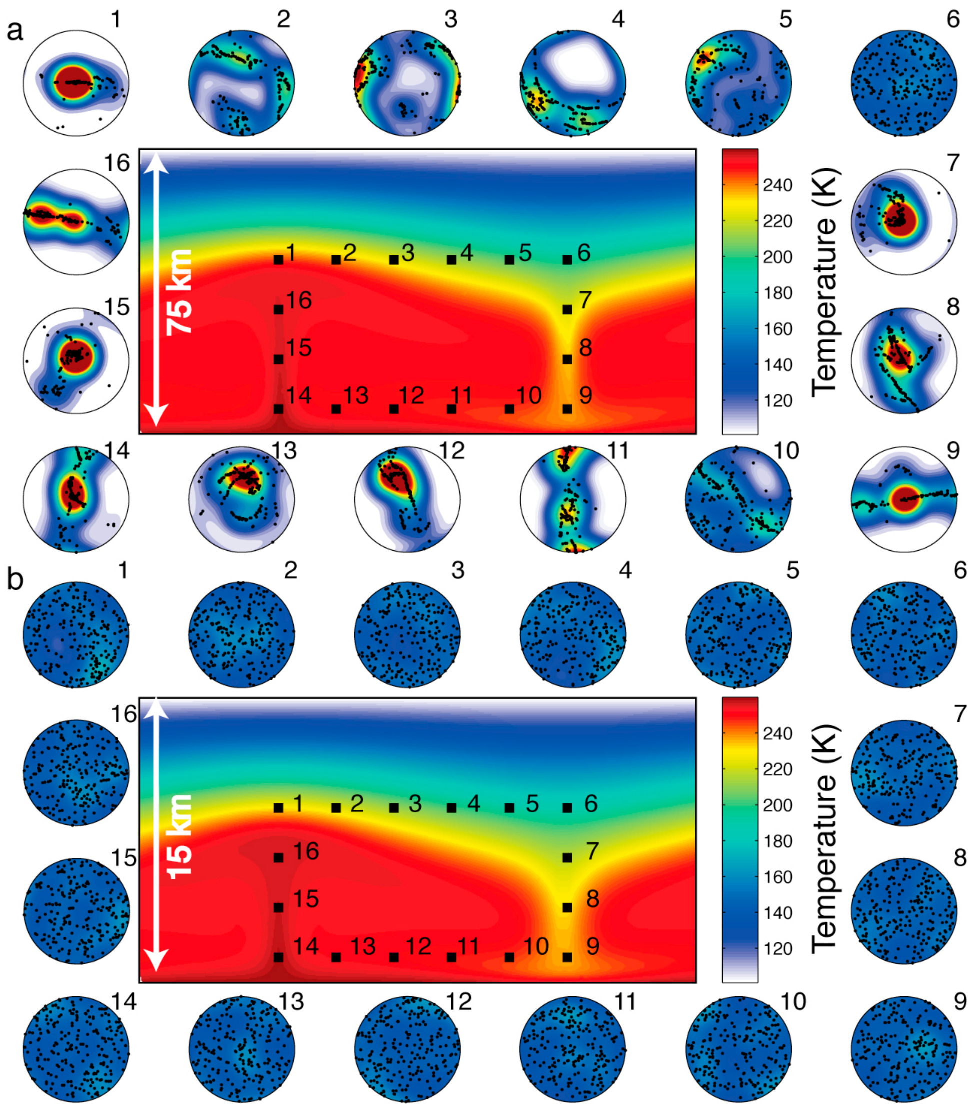

Figure 2. CPO fabrics calculated for locations marked by numbered squares in the convecting interior of the ice layer. (a) Layer thickness of 75 km, grain size 1.0 mm. (b) Layer thickness 15 km, grain size 0.1 mm.

develop in our simulations. We note that the stagnant lid is thinned locally above convective upwellings, allowing CPO to develop at shallower depths near upwellings than near downwellings, illustrated in Figure 2a. Although the lower temperature within convective downwellings promotes texture development [*Barr and Stillman*, 2011], the thickened cold thermal boundary layer above these downwellings increases the depth at which texture develops. Figure 3 shows fabrics that develop in our simulations at several depths beneath the surface. When grain size is small (0.1 mm), diffusion creep allows relatively thin ice shells to convect, but because deformation is not accommodated by dislocation creep, CPO does not develop anywhere in the ice shell, illustrated in Figure 2. If grain size is larger (1.0 mm) diffusion creep is sluggish, allowing CPO to form in the convecting interior of the ice shell (Figure 2). *Barr and Stillman* [2011] suggested that when grain size is large (1.0 mm), the entire ice shell deforms most rapidly by dislocation creep, so CPO could develop throughout the ice shell. However, we find that deformation rates in the stagnant lid are too small to produce CPO.

4. Effects of CPO on Flow Field and Heat Transport

[18] The anisotropic viscosity resulting from texture development has a first-order effect on the velocity in upwellings and downwellings (Figure 4). The more rapid flow is in agreement with studies of the effects of anisotropic viscosity on ice sheets [*Mangeney et al.*, 1996]. We calculated dynamic topography using the normal stress exerted on the upper boundary of the domain with and without texture development (Figure 4). There is negligible difference between the two simulations because, despite differences in velocity in the convecting interior, the stresses driving convection are very similar.

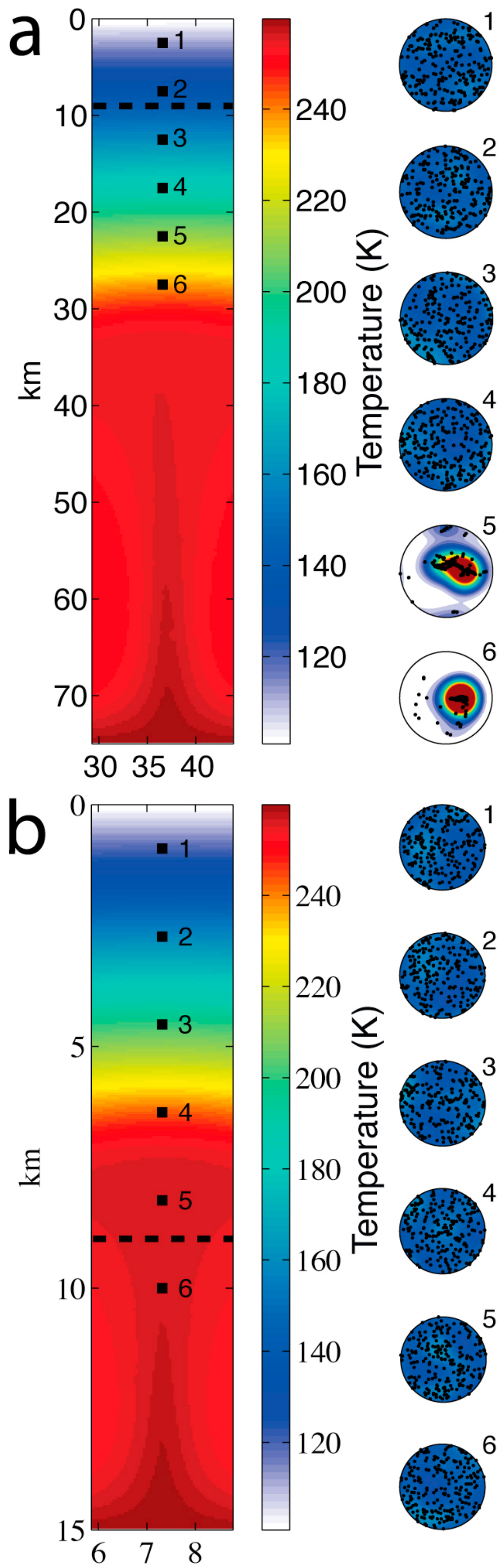

Figure 3. CPO fabrics calculated for locations marked by numbered squares, corresponding to numbered pole figures (right). Warmer colors in the pole figures indicate higher concentrations of *c* axes. Horizontal dashed lines indicate the maximum depth (9 km) to which the proposed ice-penetrating radar on the European Space Agency (ESA) JUICE spacecraft may penetrate. (a) Layer thickness of 75 km, grain size 1.0 mm. (b) Layer thickness 15 km, grain size 0.1 mm.

[19] Because it affects the velocities in upwellings and downwellings, we expect that viscous anisotropy will affect heat transport. The steady state Nusselt number achieved using the *Goldsby and Kohlstedt* [2001] rheology for Case 2 (75 km thickness) was 1.77. After enabling texture development and anisotropy, we ran the simulation for 6 Ma, at which time the Nusselt number had reached 1.94. The Nusselt number between the activation of texture development and the end of the simulation can be well approximated (R^2 = 0.9999) as an exponential function of time with the form $Nu(t) = a\exp(-bt) + c$. The term $c = 1.949 \pm 0.001$ is the expected steady state value of *Nu* (with 95% confidence bounds). Thus, the state achieved during our run had Nusselt number within 0.5% of the steady state value predicted by exponential extrapolation, and the anisotropic model transports 10% more heat than the isotropic model. We computed a steady *Nu* for anisotropic Case 1 of 1.746 ± 0.001, an increase of 5% relative to the value of 1.67 computed for the isotropic case. We expect enhanced heat transport for larger grain sizes because dislocation creep is more rapid at the smaller grain size used in Case 1. Although convective heat transport is enhanced in our model, the general uncertainty in grain size and amount of internal heating leads to much larger variations in heat transport [e.g., *Ruiz et al.*, 2007].

5. Detectability

[20] Fabric development in an ice mantle is most interesting if it produces an observable signature. Detection of CPO would imply past or ongoing deformation accommodated by specific creep mechanisms, which in turn provides insight into thermal and tectonic evolution, including constraints on grain size, stress magnitude and orientation, and strain history. A spacecraft carrying ice-penetrating radar can in principle measure preferred orientation remotely [*Barr and Stillman*, 2011]. The radar planned for European Space Agency's (ESA) JUICE spacecraft, likely the next mission to the Jovian system, is expected to be able to probe depths 100 m to 6–9 km below the surface.

[21] With a grain size of 1.0 mm, the minimum stagnant lid thickness in our isotropic simulations was 18 km (Figure 1b). With somewhat smaller grain size (0.5 mm), some CPO development may be possible (though lower texture strength is expected) and stagnant lids as thin as 14 km may develop (Figure 1c). The stagnant lids in Case 2 (75 km thickness, 1.0 mm grain size), and each of the simulations shown in Figures 1b and 1c, are sufficiently thick to preclude radar detection of CPO in the convecting interior.

[22] JUICE is expected to perform flybys of Europa and Callisto before entering orbit around Ganymede. Our calculations were performed with Europa-like $g = 1.3$ m s^{-2},

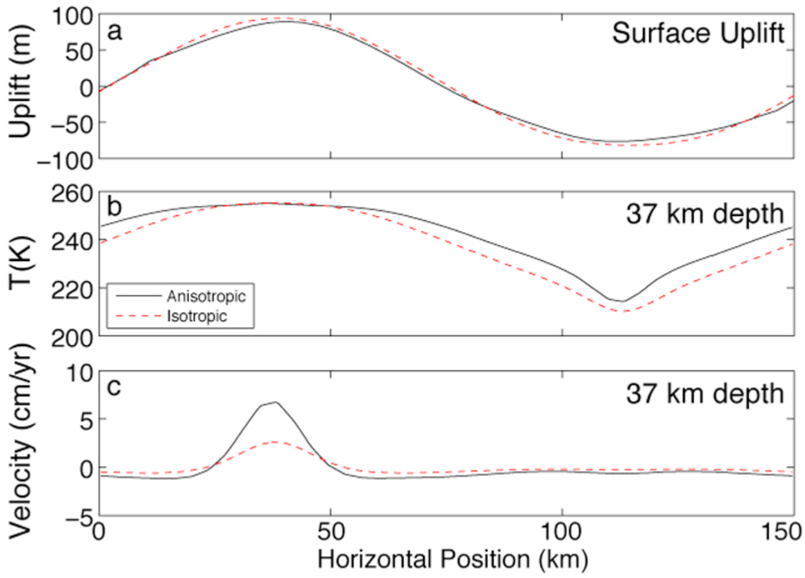

Figure 4. (a) Profiles of surface uplift (dynamic topography) for case with layer thickness 75 km and grain size $d = 1.0$ mm with (black line) and without (dashed red line) anisotropy. (b) Temperature profiles at a depth of 37 km. (c) Velocity profiles at a depth of 37 km.

but Ganymede and Callisto both have g within 10% of Europa. Because Ra is linearly proportional to g, we expect our results to be applicable to all three bodies. However, other processes not accounted for in this study could affect stagnant lid thickness, allowing texture to develop at depths where it could be detectable. In particular, plastic yielding can lead to episodic overturn of the stagnant lid [*Showman and Han*, 2005]. During overturn events, ice with CPO could be exhumed and the depth at which CPO develops could be reduced. Frictional heating on faults could lead to local temperature variations and hence localized CPO development at shallow depths [*Nimmo and Gaidos*, 2002; *Nimmo et al.*, 2007]. Internal heating by tidal dissipation could thin the stagnant lid globally, bringing CPO development nearer to the surface [*Solomatov and Moresi*, 2000; *Nimmo and Manga*, 2002, Figure 2]. Regardless of depth of formation, Figure 1a shows that deformation of polycrystalline ice with grain size >0.5 mm through strains $O(1)$ should produce CPO, and if this does occur within a few km of the surface of an icy satellite, CPO may be remotely detected.

[23] **Acknowledgments.** Computational resources were provided through the Texas Advanced Computing Center under Teragrid allocation EAR-100032 to M.L.R., by David A. Yuen at the Minnesota Supercomputing Institute, and by Bruce Buffett. We thank the Editor, Francis Nimmo, Allen McNamara, and an anonymous reviewer for their comments which improved the quality of the manuscript. We thank T. Becker, K. Cuffey, G. Hirth, and D. Kohlstedt for helpful discussions. This work was funded in part by a grant from NASA.

References

Amestoy, P. R., I. S. Duff, J.-Y. L'Excellent, and J. Koster (2001), A fully asynchronous multifrontal solver using distributed dynamic scheduling, *SIAM J. Matrix Anal. Appl.*, *23*(1), 15–41.

Amestoy, P. R., A. Guermouche, J.-Y. L'Excellent, and S. Pralet (2006), Hybrid scheduling for the parallel solution of linear systems, *Parallel Comput.*, *32*(2), 136–156.

Balay, S., J. Brown, K. Buschelman, V. Eijkhout, W. D. Gropp, D. Kaushik, M. G. Knepley, L. C. McInnes, B. F. Smith, and H. Zhang (2012), PETSc users manual, *Tech. Rep. ANL-95/11*, rev. 3.3, Argonne Natl. Lab., Argonne, Ill.

Barr, A. C., and W. B. McKinnon (2007a), Convection in Enceladus' ice shell: Conditions for initiation, *Geophys. Res. Lett.*, *34*, L09202, doi:10.1029/2006GL028799.

Barr, A. C., and W. B. McKinnon (2007b), Convection in ice I shells and mantles with self-consistent grain size, *J. Geophys. Res.*, *112*, E02012, doi:10.1029/2006JE002781.

Barr, A. C., and D. E. Stillman (2011), Strain history of ice shells of the Galilean satellites from radar detection of crystal orientation fabric, *Geophys. Res. Lett.*, *38*, L06203, doi:10.1029/2010GL046616.

Barr, A. C., R. T. Pappalardo, and S. Zhong (2004), Convective instability in ice I with non-Newtonian rheology: Application to the icy Galilean satellites, *J. Geophys. Res.*, *109*, E12008, doi:10.1029/2004JE002296.

Běhounková, M., G. Tobie, G. Choblet, and O. Čadek (2010), Coupling mantle convection and tidal dissipation: Applications to Enceladus and Earth-like planets, *J. Geophys. Res.*, *115*, E09011, doi:10.1029/2009JE003564.

Blankenbach, B., et al. (1989), A benchmark comparison for mantle convection codes, *Geophys. J. Int.*, *98*(1), 23–38.

Bunge, H. J. (1982), *Texture Analysis in Materials Science*, Butterworth, London.

Castelnau, O., P. Duval, R. A. Lebensohn, and G. R. Canova (1996), Viscoplastic modeling of texture development in polycrystalline ice with a self-consistent approach: Comparison with bound estimates, *J. Geophys. Res.*, *101*, 13,851–13,868.

Castelnau, O., G. Canova, R. Lebensohn, and P. Duval (1997), Modelling viscoplastic behavior of anisotropic polycrystalline ice with a self-Consistent approach, *Acta Mater.*, *45*(11), 4823–4834.

Castelnau, O., D. K. Blackman, and T. W. Becker (2009), Numerical simulations of texture development and associated rheological anisotropy in regions of complex mantle flow, *Geophys. Res. Lett.*, *36*, L12304, doi:10.1029/2009GL038027.

Chadwick, P. (1999), *Continuum Mechanics: Concise Theory and Problems*, 2nd ed., Dover, Mineola, N. Y.

Consolmagno, G. J., and J. S. Lewis (1978), The evolution of icy satellite interiors and surfaces, *Icarus*, *34*, 280–293.

Cuffey, K., and W. Paterson (2010), *The Physics of Glaciers*, 4th ed., Butterworth Heinemann, Burlington, Vt.

Fagents, S. A., R. Greeley, R. J. Sullivan, R. T. Pappalardo, L. M. Prockter, and The Gallileo SSI Team (2000), Cryomagmatic mechanisms for the formation of Rhadamanthys Linea, triple band margins, and other low-albedo features on Europa, *Icarus*, *144*(1), 54–88.

Freeman, J., L. Moresi, and D. A. May (2006), Thermal convection with a water ice I rheology: Implications for icy satellite evolution, *Icarus*, *180*(1), 251–264.
Gerya, T., and D. Yuen (2003), Characteristics-based marker-in-cell method with conservative finite-differences schemes for modeling geological flows with strongly variable transport properties, *Phys. Earth Planet. Inter.*, *140*(4), 293–318.
Goldsby, D. L., and D. L. Kohlstedt (2001), Superplastic deformation of ice: Experimental observations, *J. Geophys. Res.*, *106*(B6), 11,017–11,030.
Han, L., and A. P. Showman (2005), Thermo-compositional convection in Europa's icy shell with salinity, *Geophys. Res. Lett.*, *32*, L20201, doi:10.1029/2005GL023979.
Han, L. and A. P. Showman (2008), Implications of shear heating and fracture zones for ridge formation on Europa, *Geophys. Res. Lett.*, *35*, L03202, doi:10.1029/2007GL031957.
Han, L., and A. P. Showman (2010), Coupled convection and tidal dissipation in Europa's ice shell, *Icarus*, *207*(2), 834–844.
Hussmann, H., T. Spohn, and K. Wieczerkowski (2002), Thermal equilibrium states of Europa's ice shell: Implications for internal ocean thickness and surface heat flow, *Icarus*, *156*(1), 143–151.
Lebensohn, R., and C. Tome (1993), A self-consistent anisotropic approach for the simulation of plastic deformation and texture development of polycrystals: Application to zirconium alloys, *Acta Metall. Mater.*, *41*(9), 2611–2624.
Leng, W., and S. Zhong (2011), Implementation and application of adaptive mesh refinement for thermochemical mantle convection studies, *Geochem. Geophys. Geosyst.*, *12*, Q04006, doi:10.1029/2010GC003425.
Manga, M., and C.-Y. Wang (2007), Pressurized oceans and the eruption of liquid water on Europa and Enceladus, *Geophys. Res. Lett.*, *34*, L07202, doi:10.1029/2007GL029297.
Mangeney, A., F. Califano, and O. Castelnau (1996), Isothermal flow of an anisotropic ice sheet in the vicinity of an ice divide, *J. Geophys. Res.*, *101*(B12), 28,189–28,204.
McKinnon, W. B. (1999), Convective instability in Europa's floating ice shell, *Geophys. Res. Lett.*, *26*(7), 951–954.
Mitri, G., and A. P. Showman (2005), Convective-conductive transitions and sensitivity of a convecting ice shell to perturbations in heat flux and tidal-heating rate: Implications for Europa, *Icarus*, *177*(2), 447–460.
Mitri, G., and A. P. Showman (2008), A model for the temperature-dependence of tidal dissipation in convective plumes on icy satellites: Implications for Europa and Enceladus, *Icarus*, *195*(2), 758–764.
Moore, W. B. (2006), Thermal equilibrium in Europa's ice shell, *Icarus*, *180*(1), 141–146.
Nimmo, F., and E. Gaidos (2002), Strike-slip motion and double ridge formation on Europa, *J. Geophys. Res.*, *107*(E4), 5021, doi:10.1029/2000JE001476.
Nimmo, F., and M. Manga (2002), Causes, characteristics and consequences of convective diapirism on Europa, *Geophys. Res. Lett.*, *29*(23), 2109, doi:10.1029/2002GL015754.
Nimmo, F., J. R. Spencer, R. T. Pappalardo, and M. E. Mullen (2007), Shear heating as the origin of the plumes and heat flux on Enceladus, *Nature*, *447*(7142), 289–291.
Pappalardo, R. T., and A. C. Barr (2004), The origin of domes on Europa: The role of thermally induced compositional diapirism, *Geophys. Res. Lett.*, *31*, L01701, doi:10.1029/2003GL019202.
Pappalardo, R. T., et al. (1998), Geological evidence for solid-state convection in Europa's ice shell, *Nature*, *391*, 365–368.
Rathbun, J. A., G. S. Musser Jr., and S. W. Squyres (1998), Ice diapirs on Europa: Implications for liquid water, *Geophys. Res. Lett*, *25*(22), 4157–4160.
Roberts, J. H., and F. Nimmo (2008), Tidal heating and the long-term stability of a subsurface ocean on Enceladus, *Icarus*, *194*(2), 675–689.
Rudolph, M. L., and M. Manga (2009), Fracture penetration in planetary ice shells, *Icarus*, *199*(2), 536–541.
Ruiz, J. (2010), Equilibrium convection on a tidally heated and stressed icy shell of Europa for a composite water ice rheology, *Earth Moon Planets*, *107*(2-4), 157–167.
Ruiz, J., and R. Tejero (2003), Heat flow, lenticulae spacing, and possibility of convection in the ice shell of europa, *Icarus*, *162*(2), 362–373.
Ruiz, J., J. A. Alvarez-Gómez, R. Tejero, and N. Sánchez (2007), Heat flow and thickness of a convective ice shell on Europa for grain size-dependent rheologies, *Icarus*, *190*(1), 145–154.
Schenk, P. M., and R. T. Pappalardo (2004), Topographic variations in chaos on Europa: Implications for diapiric formation, *Geophys. Res. Lett.*, *31*, L16703, doi:10.1029/2004GL019978.
Showman, A. P., and L. Han (2004), Numerical simulations of convection in Europa's ice shell: Implications for surface features, *J. Geophys. Res.*, *109*, E01010, doi:10.1029/2003JE002103.
Showman, A. P., and L. Han (2005), Effects of plasticity on convection in an ice shell: Implications for Europa, *Icarus*, *177*(2), 425–437.
Solomatov, V. (1995), Scaling of temperature- and stress-dependent viscosity convection, *Phys. Fluids*, *7*(2), 266–274.
Solomatov, V. S., and L. N. Moresi (2000), Scaling of time-dependent stagnant lid convection: Application to small-scale convection on Earth and other terrestrial planets, *J. Geophys. Res.*, *105*, 21,795–21,818.
Sotin, C., J. W. Head III, and G. Tobie (2002), Europa: Tidal heating of upwelling thermal plumes and the origin of lenticulae and chaos melting, *Geophys. Res. Lett.*, *29*(8), 1233, doi:10.1029/2001GL013844.
Taylor, G. I. (1938), Plastic strain in metals, *J. Inst. Metals*, *62*, 307–324.
Thorsteinsson, T. (2002), Fabric development with nearest-neighbor interaction and dynamic recrystallization, *J. Geophys. Res.*, *107*(B1), 2014, doi:10.1029/2001JB000244.
Tobie, G., G. Choblet, and C. Sotin (2003), Tidally heated convection: Constraints on Europa's ice shell thickness, *J. Geophys. Res.*, *108*(E11), 5124, doi:10.1029/2003JE002099.
Travis, B. J., J. Palguta, and G. Schubert (2012), A whole-moon thermal history model of Europa: Impact of hydrothermal circulation and salt transport, *Icarus*, *218*(2), 1006–1019.